ACS OMEGA

Article

Cite This: ACS Omega 2017, 2, 9250−9260

Probing the Critical Role of Sn Content in SnSb@C Nanofiber Anode on Li Storage Mechanism and Battery Performance

Suman Das, Tayur N. Guru Row,* and Aninda J. Bhattacharyya*

Solid State and Structural Chemistry Unit, Indian Institute of Science, Bangalore 560012, India

Supporting Information

ABSTRACT: The minimization of the detrimental effects as a result of the drastic volume changes (few hundred times) occurring during repeated alloying−dealloying of lithium with group IV elements, e.g., tin (Sn), is a major challenge. An important design strategy is to have Sn as a component in a binary compound. SnSb is an important example where the antimony (Sb) itself is redox active at a potential higher than that of Sn. The ability of Sb to alloy with Li reduces the Li uptake amount of Sn in SnSb compared to that in bare Sn. Thus, the volume changes of Sn in SnSb will expectedly be much lower compared to that in bare Sn, leading to greater mechanical stability and cyclability. As revealed recently, the complete reformation of SnSb (for a molar ratio of Sn/Sb = 1:1) during charging is not achieved due to the loss of some fraction of Sn. Thus, the molar concentration of Sn and Sb in SnSb is also absolutely important for the optimization of battery performance. We discuss here SnSb with varying compositions of Sn encapsulated inside an electrospun carbon nanofiber (abbreviated as CF). The carbon-nanofiber matrix not only provides electron transport pathways for the redox process but also provides ample space to accommodate the drastic volume changes occurring during successive charge and discharge cycles. The systematic changes in the chemical composition of SnSb minimize the instabilities in SnSb structure as well as replenish any loss in Sn during repeated cycling. The composition plays a very crucial role, as magnitude of specific capacities and cyclability of SnSb are observed to depend on the variable percentage of Sn. SnSb-75-25-CF, which contains excess Sn, exhibits the highest specific capacity of 550 mAh g^{-1} after 100 cycles in comparison with pure SnSb (1:1) anode material at a current density of 0.2 A g^{-1} and shows excellent rate capability over widely varying current densities (0.2−5 A g^{-1}).

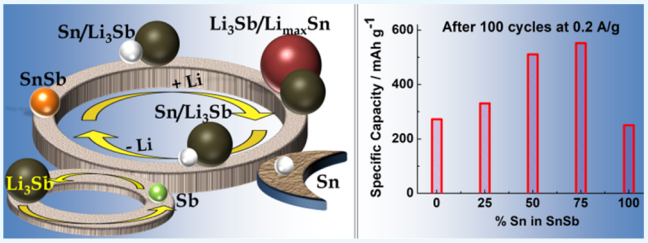

INTRODUCTION

There has been a progressive shift in long-term strategies to harness and store energy from renewable natural sources, e.g., solar, wind, and hydro.[1] This is expected to have 2-fold benefits. First, the shift to renewables will decrease mankind's dependence on fossil fuels and related technologies. Second, the usage of renewable technologies will pave the way for better preservation of the global environment and lead to sustainable growth. Strategies based on energy harvesting and storage via electrochemical means have gained substantial momentum over the last several decades. Energy storage using rechargeable batteries, e.g., alkali-based rechargeable batteries, viz., Li-ion battery, have already demonstrated several high-value opportunities for a wide range of applications.[2] Lithiated transition metal oxides (e.g., $LiCoO_2$) and graphite have been used as cathode and anode materials in conventional intercalation-based lithium-ion batteries.[3] However, the above combination of electrode materials displays limited capabilities for applications beyond small mobile electronic devices. In the case of graphite or as a matter of fact for other carbon forms, e.g., carbon nanotube, fullerene, graphene, and hierarchical carbon, operation at higher current densities leads to degradation of the conventional liquid carbonate mixture electrolyte, leading to an unstable solid electrolyte interface (SEI) and poor cyclability. Additionally, the rapid growth rate of lithium dendrites on the electrode surface compromises operational safety.[4,5] To enhance the energy density and safety of the battery at high current densities, materials supporting higher number of exchangeable lithium at higher redox voltage are necessary. Elements of group IV, viz., silicon (Si), germanium (Ge), and tin (Sn), have the potential to form alloy with lithium and store >4 Li^+ during charge−discharge processes (vis-à-vis graphite = 0.5 Li^+).[6,7] Si has attracted tremendous interest from both academia and industry, primarily due to its extraordinarily high specific capacity of 3500 mAh g^{-1} (volumetric capacity ∼ 2190 mAh cm^{-3}).[8] On the other hand, Sn is an equally interesting and important alloying element. Sn delivers a lower specific capacity (≈1000 mAh g^{-1}) compared to that of Si (≈3500 mAh g^{-1}). However, this disadvantage is offset by the high thermal stability, high electrical conductivity, and high volumetric capacity (∼1991 mAh cm^{-3}) of Sn.[7,9] All of these material properties make Sn a unique anode material for lithium-based batteries.

Received: October 4, 2017
Accepted: December 13, 2017
Published: December 27, 2017

DOI: 10.1021/acsomega.7b01479
ACS Omega 2017, 2, 9250−9260

The major issue with the alloying mode of energy storage is the enormous volume changes taking place during discharge and charge of the battery. These volume changes severely affect the integrity of the particle structure and morphology, resulting in a rapid rate of capacity fading.[10,11] To circumvent the volume changes, several design strategies based on composites of Sn with carbon have been developed.[12−19] The main purpose here is to minimize the particle degradation via optimization of the Sn particle architecture and Sn interparticle distance, with the carbon acting as the electronic conduit for the relevant redox process. Another important strategy for tackling volume changes has been to synthesize binary compounds of Sn. Binary compounds that have been investigated include $CoSn_3$,[20] Ni_3Sn_4,[21] Cu_6Sn_5,[22] and SnSb.[23−37] The basis for selection of a binary compound instead of Sn is essentially to buffer the drastic volume changes occurring as a result of excessive Li (≥4.4) storage. In the case of SnSb (molar ratio 1:1), both Sn and Sb can alloy with lithium. Sb takes up some amount of lithium and undergoes lithiation at a higher potential. This reduces the Li uptake amount of Sn in SnSb compared to that in bare Sn. Thus, the volume changes of Sn in SnSb will expectedly be much lower compared to those in bare Sn, leading to greater mechanical stability and cyclability. To the best of our knowledge, the effect of molar percentage of Sb on the electrochemical performance is not reported in the literature. Recently, in operando synchrotron X-ray diffraction coupled with Mössbauer spectroscopy has demonstrated the loss of fraction of Sn in SnSb (1:1) on each charging.[38] In this regard, the variation in composition of SnSb can be interesting as this may lead to optimization of the molar ratios of Sn and Sb in SnSb, which may result in a superior Sn-based anode for commercial batteries.

Herein, we report an anode comprising of varying compositions of Sn in SnSb entrapped inside an electrospun carbon fiber host (abbreviated C-fiber). The carbon fiber provides both electron conducting pathways and also free space for accommodating the volume changes during charge−discharge cycling. Varying compositions of SnSb inside the C-fiber host is an additional advantage, as it can be used for tuning the electrochemical performance. Excess Sn in SnSb leads to some interesting implications in terms of electrochemical properties and enhances the performance of the material compared to that of the reported SnSb with equal molar concentrations of Sn and Sb.

RESULTS AND DISCUSSION

Lithiation of SnSb (1:1) particles, which is referred to here as the SnSb-50-50-CF sample (vide infra), occurs via the following mechanisms[38]

$$SnSb + 3Li \rightarrow Li_3Sb + Sn \quad (1)$$

$$Sn + 0.4Li \rightarrow 0.2Li_2Sn_5 \quad (2)$$

$$0.2Li_2Sn_5 + 0.6Li \rightarrow LiSn \quad (3)$$

$$LiSn + (y-1)Li \rightarrow Li_ySn(y \sim 2.5) \quad (4)$$

$$Li_ySn(y \sim 2.5) + (\max - y)Li \rightarrow Li_{max}Sn \quad (5)$$

whereas the delithiation occurs via the following steps

$$Li_{max}Sn \rightarrow Li_ySn(y \sim 2.5) + (\max - y)Li \quad (6)$$

$$Li_ySn(y \sim 2.5) \rightarrow LiSn + (y-1)Li \quad (7)$$

$$LiSn \rightarrow 0.2Li_2Sn_5 + 0.6Li \quad (8)$$

$$0.2Li_2Sn_5 \rightarrow Sn + 0.4Li \quad (9)$$

$$Li_3Sb + Sn \rightarrow SnSb + 3Li \quad (10)$$

$$Li_3Sb \rightarrow Sb + 3Li \quad (11)$$

Scheme 1a summarizes the various phases of SnSb formed during discharge and charge processes, respectively. On full

Scheme 1. (a) Schematic Depiction of the Lithiation and Delithiation Mechanism in SnSb and (b, c) Illustration of the Mechanism of the Electrospinning Synthesis of Particles Embedded inside Carbon Nanofibers

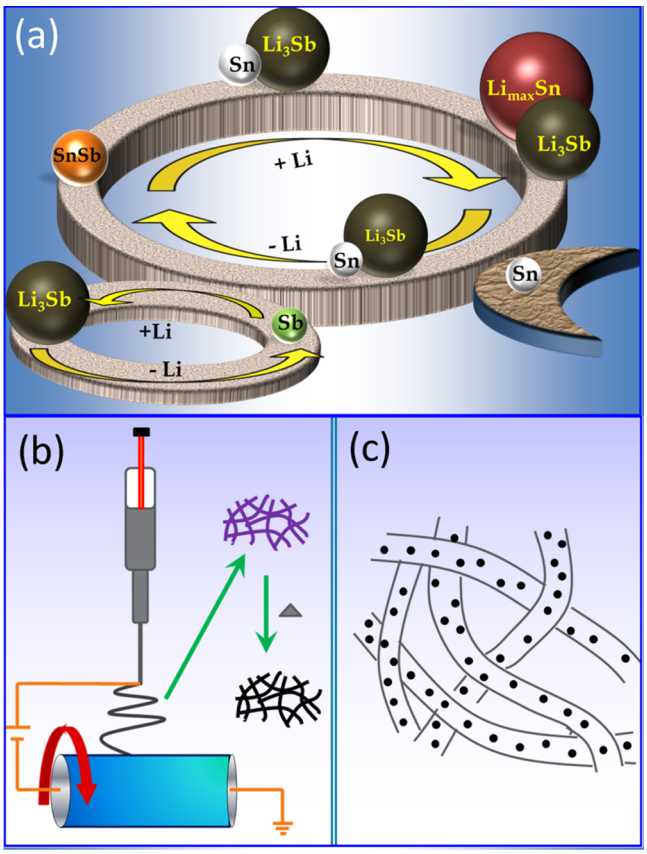

lithiation, SnSb (1:1) converts to mixture of Li_3Sb and Li_xSn (or $Li_{max}Sn$, cf. lithiation steps, eqs 1, 2, 3, 4, and 5). However, the conversion back to SnSb from the lithiated phase (Li_3Sb and Li_xSn) is not complete and amounts to loss of some fraction of Sn. This results in remnant amounts of Li_3Sb, which converts to Sb in due course of the charging process (cf. delithiation step, eq 11). Thus, loss of Sn from SnSb persists as a major issue for capacity fading and commercialization of SnSb as an anode for Li-ion battery. With this view in mind, we investigate the electrochemical storage properties of SnSb with varying contents of Sn. It is anticipated that higher concentration of Sn in SnSb will be highly beneficial in minimization of the irreversible loss of Sn, which is the key component in SnSb, leading to stable cyclability at widely varying current densities. Additionally, the SnSb particles are encapsulated here inside C nanofibers, which provide both

DOI: 10.1021/acsomega.7b01479
ACS Omega 2017, 2, 9250−9260

electron transport pathways as well as accommodate the drastic volume changes occurring during the successive charge−discharge cycling. Scheme 1b,c shows the electrospinning method, which is a versatile synthesis tool for the generation of useful one-dimensional nanostructures with uniform diameters containing the metal particles embedded inside it.

Figure 1 shows the powder X-ray diffraction (XRD) pattern of the as-synthesized SnSb particles, with a varying molar

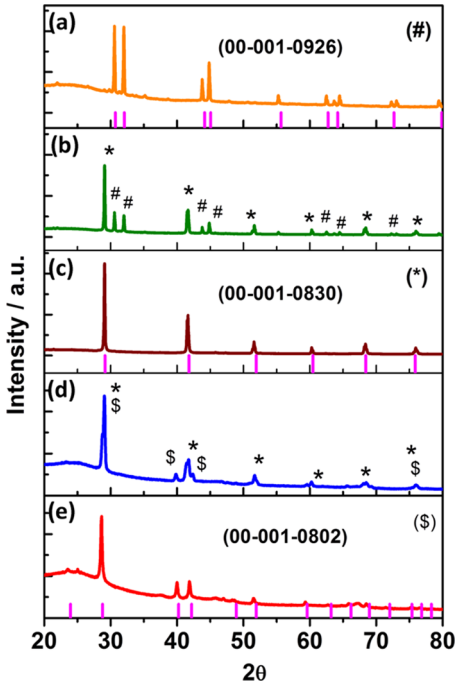

Figure 1. Powder X-ray diffraction pattern of (a) Sn-CF, (b) SnSb-75-25-CF, (c) SnSb-50-50-CF, (d) SnSb-25-75-CF, and (e) Sb-CF. The vertical lines in (a, c, and e) represent the reference pattern of Sn, SnSb, and Sb, respectively. The reference data are mentioned in respective boxes.

composition of Sn encapsulated inside the carbon nanofiber, in the range 2θ = 20−80°. The powder X-ray diffraction pattern of Sn-CF in Figure 1a matches exactly with the reference pattern (JCPDS reference code: 00-001-0926, indicated by the vertical lines). This proves that Sn particles inside the carbon nanofibers are in the metallic state in the tetragonal crystal system and $I4_1/amd$ space group. Figure 1c,e corresponds to the powder X-ray diffraction pattern of as-synthesized SnSb-50-50-CF and Sb-CF compounds. They match well with the respective reference patterns of the binary alloy SnSb (reference code: 00-001-0830) and metallic Sb (reference code: 00-001-0802) particles, indicating formation of high-purity compounds. Both SnSb-50-50-CF and Sb-CF compounds crystallize in the rhombohedral crystal system.

The powder X-ray diffraction pattern of SnSb-75-25-CF (Figure 1b) is a combination of diffraction peaks of SnSb (marked as *) and Sn (marked as $^{\#}$), indicating an intimate mixture of Sn and SnSb. Similarly, the powder X-ray diffraction pattern of SnSb-25-75-CF is assigned as a combination of diffraction peaks due to SnSb (marked as *) and Sb (marked as $^{\$}$) particles. The sharp peaks appearing for all patterns indicate that the samples are generally crystalline in nature. The diffraction patterns of carbon present in the C-nanofiber−SnSb samples do not show up in the powder XRD pattern as it is in the amorphous form. This is evident from the broad background observed in the powder X-ray diffraction patterns. To investigate the thermal stability of the as-synthesized samples, thermogravimetric analysis (TGA) is carried out under oxygen atmosphere in the temperature range (30−700 °C) (Figure 2). The percentages of carbon present in the samples can be determined from the weight loss around 470 °C. The carbon content in the samples is found to vary in the range of 44% (SnSb-75-25-CF) to 55% (Sn-CF) implying the SnSb contents to be in the range of 56−45%. To investigate the extent of carbonization of the as-synthesized compounds from their respective polymer fiber precursors, Fourier transform infrared (FTIR) spectra are recorded for all samples viz. Sn-CF (Figure 3a), SnSb-75-25-CF (Figure 3b), SnSb-50-50-CF (Figure 3c), SnSb-25-75-CF (Figure 3d), Sb-CF (Figure 3e), and polyacrylonitrile (PAN) fiber (Figure 3f). The spectrum for PAN displays a characteristic band at 2250 cm^{-1} that can be assigned to the stretching of the nitrile group. The band at 1663 cm^{-1} is assigned to C═O stretch, whereas the absorption bands in the range 1000−1500 cm^{-1} are due to C−H stretching.[39,40] Compared to PAN, the spectra of the various SnSb compounds (Figure 3a−e) do not exhibit any of the significant bands of the polymer. This strongly indicates the complete carbonization of PAN.

As-synthesized compounds are further characterized by Raman spectroscopy (Figure S1) specifically to ascertain the nature of carbon formed in the C-nanofiber−SnSb samples. The characteristic signature bands around 1600 and 1360 cm^{-1} corresponding to the G-mode and D-mode of vibrations of sp^2 carbons indicate the graphitic nature of the carbon formed from the polymer decomposition.[41] To investigate the morphology of the samples, scanning electron microscopy (SEM) and transmission electron microscopy (TEM) studies have been carried out. Figure S2a shows the representative scanning electron micrograph of the electrospun polymer fibers containing different concentrations of $SnCl_2$ and $SbCl_3$. The width of the polymer fibers ranges from (100−180 nm), with average thickness of 130 nm (represented by the histogram in the inset of Figure S2a). The length of the fibers is found to be more than several micrometers.

Figure S2b represents the SEM image of the fibers after carbonization of PAN to carbon nanofibers. It is to be noticed here that the carbonization results in the breaking of long nanofibers into shorter fibers with nearly the same thickness. Transmission electron microscopy image (Figure 4a) clearly shows the SnSb particles embedded inside the carbon nanofibers. The encapsulation of the particles inside the carbon nanofibers is shown in Figure 4b−f. The average particle size of the SnSb particles is around 15−20 nm for all of the composites except SnSb-25-75-CF, which exhibits particles of smaller size ≈5−7 nm embedded inside the C fiber. The embedded particles are crystalline in nature. This is evident from the lattice fringes observed in the high-resolution TEM (HRTEM) image (Figure S3) and its corresponding fast Fourier transformation (FFT). The FFT shows spots indicating the crystallinity of the particles. The FFT corresponding to the carbon fiber region (marked with a yellow dashed box) is devoid of any spots, implying the amorphous nature of the carbon fibers.

The electrochemical properties of as-synthesized compounds are investigated using cyclic voltammetry. The Li metal acts as both the reference and counter electrode, and a scan rate of 0.1 mV s^{-1} and a potential window of 0.05−2 V

DOI: 10.1021/acsomega.7b01479
ACS Omega 2017, 2, 9250−9260

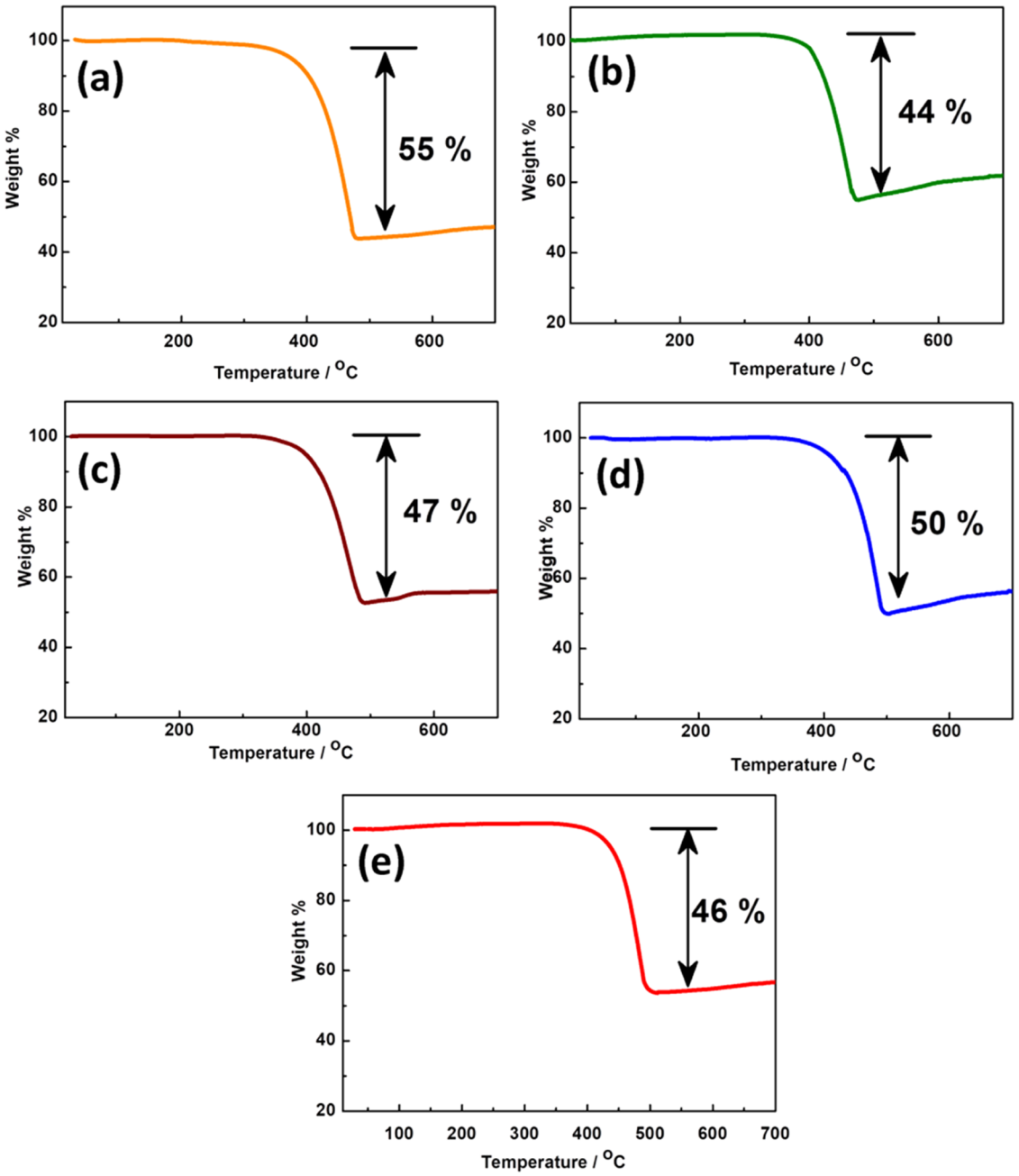

Figure 2. Thermogravimetric analysis (TGA) of (a) Sn-CF, (b) SnSb-75-25-CF, (c) SnSb-50-50-CF, (d) SnSb-25-75-CF, and (e) Sb-CF.

are chosen for the cyclic voltammetry. Figure S4a represents the cyclic voltammogram of Sb-CF versus $Li^+|Li$. The first cathodic scan displays a broad peak containing two small peaks at 0.7 and 0.6 V. These are attributed, respectively, to the lithiation of Sb to form Li_3Sb and formation of a solid electrolyte interface (SEI) due to electrolyte degradation on the electrode surface. From the second cycle, the SEI peak at 0.6 V is not observed, indicating that no further electrolyte degradation takes place, leading to a stable SEI interface layer.

From the second cycle, the lithiation of Sb occurs at a slightly higher voltage (0.8 V) compared to that in the first cathodic scan. The peak at 1.06 V in the anodic scan is attributed to delithiation of Li_3Sb to form metallic Sb. Figure S4b shows the galvanostatic charge−discharge cycling profiles (0.2 A g^{-1}) of Sb-CF versus $Li^+|Li$ in the potential range 0.05−2.0 V. A sharp drop in the specific capacity is observed from the first to the second cycle, following which the stable cycling is obtained. The voltage plateaus obtained at 0.8 and 1.1 V in discharge and charge runs are well in accordance with the redox signatures obtained from the cyclic voltammograms. Figure S4c,d represents the galvanostatic charge−discharge voltage profiles and the corresponding specific capacity retention over charge−discharge cycles versus $Li^+|Li$, as a function of increasing current rate densities. The Sb-CF cell delivered a stable capacity of 300 mAh g^{-1} (versus $Li^+|Li$) at the end of 20 cycles at 0.2 A g^{-1} and a reasonably good specific capacity of 130 mAh g^{-1} at 5 A g^{-1}. On reverting to 0.2 A g^{-1}, the cell delivered a specific capacity of 260 mAh g^{-1}. In the case of SnSb-25-75-CF, due to excess Sb phase along with SnSb, the electrochemical behavior resembles that of Sb-CF fiber. The first cathodic scan in cyclic voltammogram (Figure S5a) is mainly due to the contribution of carbon and formation

DOI: 10.1021/acsomega.7b01479
ACS Omega 2017, 2, 9250−9260

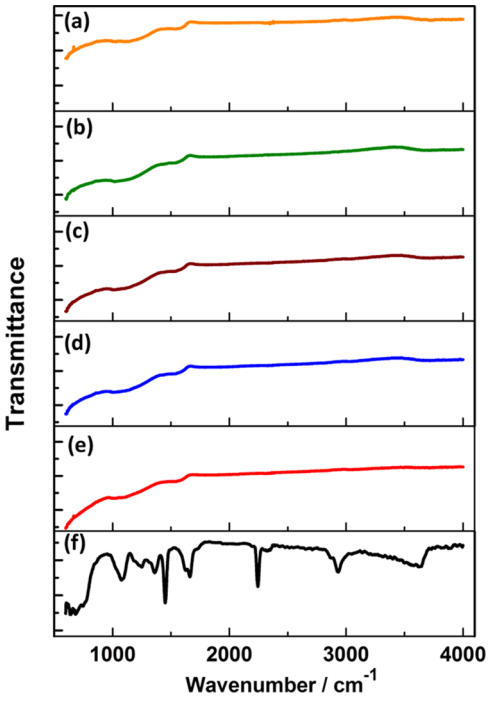

Figure 3. Fourier transform infrared (FTIR) spectra of (a) Sn-CF, (b) SnSb-75-25-CF, (c) SnSb-50-50-CF, (d) SnSb-25-75-CF, (e) Sb-CF, and (f) polyacrylonitrile (PAN).

of stable SEI formation. The SEI once formed remains stable, and its signature peak does not reappear in the subsequent cycles. From the second cycle, the peak at 0.8 V in the cathodic scan is attributed to the lithiation of SnSb and Sb phase to form Li_3Sb and Sn. Peaks in the range of 0.6−2.4 V are due to multiphasic lithiation of Sn, which on oxidation again produces Sn at 0.66 V. This is followed by the generation of Sb at 1.1 V to form SnSb and extra Sb in the anodic scan. Figure S5b,c represents, respectively, the galvanostatic charge−discharge voltage profile of SnSb-25-75-CF versus $Li^+|Li$ at a current density of 0.2 A g^{-1} versus successive cycles and the second cycle discharge as a function of various current densities, 0.2−5.0 A g^{-1}, in the voltage range of 0.05−2.0 V, respectively. At 0.2 A g^{-1}, SnSb-25-75-CF delivers a specific capacity of 320 mAh g^{-1} at the end of 20 cycles, and at 5 A g^{-1}, it delivers 114 mAh g^{-1}. On reverting to 0.2 A g^{-1}, 300 mAh g^{-1} of specific capacity could be achieved at the end of 100 cycles of charge and discharge (Figure S5d). On increasing the Sn content in the precursor from 25:75 (as in SnSb-25-75-CF) to 50:50 in SnSb-50-50-CF, no electrochemical signatures related to Sb (as in SnSb-25-75-CF) or Sn (as in SnSb-75-25-CF, vide infra) are observed. The cyclic voltammetry of SnSb-50-50-CF versus $Li^+|Li$ at a scan rate of 0.1 mV s^{-1} is depicted in Figure 5a. The first cathodic scan in the cyclic voltammogram contains a peak at 0.6 V, which may be attributed to lithiation of SnSb to form Li_3Sb and Sn and formation of SEI on the electrode surface. Four small peaks in the range of 0.5−0.2 V are attributed to the multiphasic Sn−Li alloy formation (steps 2−5 of lithiation of SnSb). The first anodic scan contains five closely spaced peaks between 0.7 and 1.1 V. The first three peaks (approximately 0.68, 0.78, and 0.83 V) correspond to delithiation of Sn−Li alloy. Peaks at approximately 1.08 and 1.14 V are due to the delithiation of Li_3Sb in the presence of Sn to form SnSb and slight excess of Li_3Sb to form Sb. These redox steps have been highlighted as a drawback of SnSb (1:1), as some fraction of Sn becomes unavailable in successive cycles, thus leading to a capacity lower than the theoretical capacities. From the second cathodic scan, the first lithiation peak in SnSb shifted to approximately 0.8 V and attributed to the generation of Li_3Sb (also seen in the Sb-CF sample) and Sn phase. This is followed by the multiphasic lithiation process of Sn and appears as a broader peak in the range of 0.5−0.2 V. The first anodic scan (followed by the first cathodic scan) onward, the oxidation and reduction peaks positions remain the same in the consecutive cycles. Figure 5b,c shows the galvanostatic charge−discharge voltage profile of SnSb-50-50-CF versus $Li^+|Li$ at a current density of 0.2 A g^{-1} for different cycle numbers and rate capability in the current range 0.2−5.0 A g^{-1} (for second cycles only). SnSb-50-50-CF versus $Li^+|Li$ delivers a stable specific capacity of 580 mAh g^{-1} at the end of 20 cycles at 0.2 A g^{-1} and 250 mAh g^{-1} at 5 A g^{-1}. On reverting to 0.2 A g^{-1}, a capacity of 520 mAh g^{-1} is obtained, which is in close proximity to capacities obtained in the initial run.

When the relative molar ratio of Sn to Sb increased from 50:50 to 75:25 in compound SnSb-75-25-CF, the electrochemical redox signatures shifted toward that of Sn. Figure 6 represents the electrochemical properties of SnSb-75-25-CF versus $Li^+|Li$. The first cathodic scan in the cyclic voltammogram (Figure 6a) is dominated by lithiation into the carbon fiber and SnSb phase. At the lower voltage ranges, the peaks at approximately 0.45, 0.37, and 0.24 V are attributed to the multiphasic alloy formation between Sn and Li. In the first anodic run, similar redox peaks are observed as those in SnSb-50-50-CF compound. Peaks at approximately 0.68, 0.77, and 0.83 V represent multiphasic delithiation of Sn−Li alloy, and the peak at approximately 1.1 V is attributed to delithiation of Li_3Sb to form SnSb in the presence of Sn. Figure 6b represents the galvanostatic charge−discharge voltage profiles for different cycle numbers at a constant current density (0.2 A g^{-1}). The rate capability of this material has been tested at different current densities ranging from 0.2−5.0 A g^{-1}, and the corresponding specific capacities obtained have been represented in Figure 6d. Initially, the cell provides a specific capacity of 615 mAh g^{-1} at a current density of 0.2 A g^{-1} after 20 cycles. On increasing the current density stepwise, the cell provides a specific capacity of 265 mAh g^{-1} at 5.0 A g^{-1}. The specific capacity recovered to 560 mAh g^{-1} following the revert to 0.2 A g^{-1}. The electrochemical properties of Sn-CF versus $Li^+|Li$ have been represented in Figure S6. The cyclic voltammogram (Figure S6a) of Sn-CF shows peaks at approximately 0.52, 0.42, and 0.24 V in the first cathodic scan, which is attributed to the formation of SEI and lithiation of Sn to form Sn−Li alloy. The first anodic scan has the redox peaks at approximately 0.51 and 0.69 V, which are due to the delithiation of Sn−Li alloy. The broad peak at approximately 1.2 V is attributed to the delithiation from the partially disordered nature of the carbon of the carbon fiber.[42] Figure S6b,c represents the galvanostatic charge−discharge voltage profile in the voltage range 0.05−2.0 V at a current density of 0.2 A g^{-1}, with increasing cycle numbers, and at second discharge cycle, with increasing current density of 0.2−3.0 A g^{-1}, respectively. The capacity value obtained in the rate capability test is 358 mAh g^{-1} after 20 cycles at 0.2 A g^{-1}, and with stepwise increase in the current rate, 119 mAh g^{-1} specific capacity can be achieved at 3.0 A g^{-1}. Further, on setting the current rate to its initial value (=0.2 A g^{-1}), the cell delivers a capacity of 256 mAh g^{-1} after 100 cycles (Figure S6d).

DOI: 10.1021/acsomega.7b01479
ACS Omega 2017, 2, 9250−9260

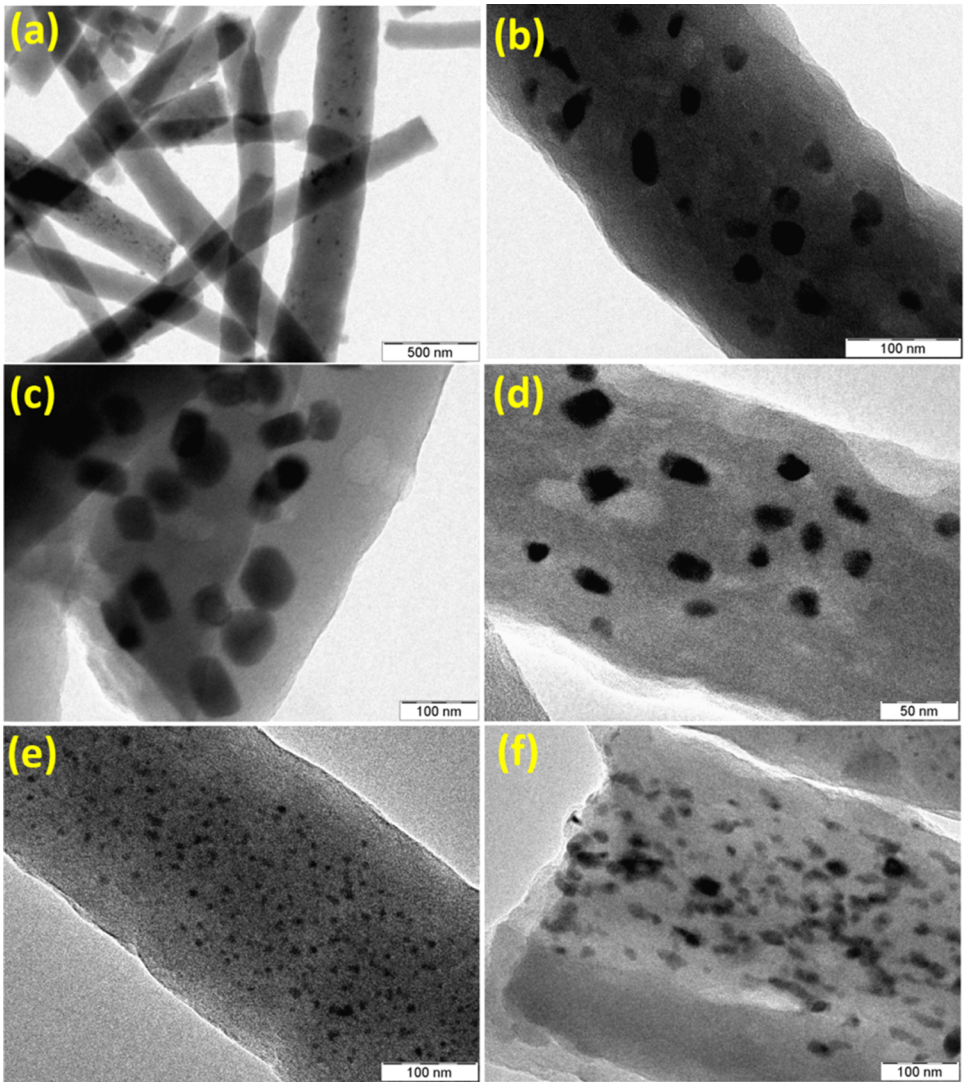

Figure 4. (a) Representative transmission electron micrograph of SnSb particles embedded inside C nanofibers (lower magnification). Transmission electron microscopy images of (b) Sn-CF, (c) SnSb-75-25-CF, (d) SnSb-50-50-CF, (e) SnSb-25-75-CF, and (f) Sb-CF, respectively.

To investigate the long-term cyclability of the series of the as-synthesized compounds, the cells are subjected to discharge and charge at a constant current of 0.2 A g^{-1} in the potential window of 0.05−2.0 V. As shown in Figure 6c, all of the cells undergo an initial irreversible capacity loss in the first discharge; however, from the second cycle onward, the losses diminish quite significantly. The irreversible capacity loss from the first to the second cycle is mainly attributed to the formation of the SEI. This is also observed in the cyclic voltammograms, where following the first cathodic scan, the redox peaks in both cathodic and anodic scans are nearly reversible with increasing cycle numbers and correspond to the redox activity of metal particles with lithium. This implies that the charge storage mainly takes place in the metal particles and not in the carbon fibers. Figure 6c shows the capacity fading is most prominent in Sn-CF compared to that in the other compounds. Second discharge capacity of Sn-CF is 501 mAh g^{-1}, which is reduced to 329 mAh g^{-1} at the 50th cycle, implying capacity fading of 34% with respect to the second discharge cycle. The capacity gradually decreases with cycling, and at the 100th cycle it is found to be 250 mAh g^{-1}, implying a further capacity fade of 24% in 50−100 cycles of galvanostatic charge−discharge in Sn-CF. However, in the case of Sb-CF, the capacity fading is less prominent, being nearly 23% in the first 50 cycles (with respect to second discharge capacity, 391 mAh g^{-1}) and nearly 9.3% between 50 and 100 cycles. This is mainly due to the lower volume expansion of Sb (200%) with respect to Sn (260%) and lower amount of lithium storage in the discharge process against $Li^+|Li$.[43] After 100 cycles, Sb-CF displays a discharge capacity of 272 mAh g^{-1}. In the case of SnSb-25-75-CF, an almost similar trend of capacity retention is observed and the specific capacity is found to be 331 mAh g^{-1} after 100 cycles, which is higher than that of the Sb-CF (and Sn-CF), as expected due to the presence of the SnSb phase.

In the case of SnSb-50-50-CF, stable capacities of 535 and 511 mAh g^{-1} are observed at the 50th and 100th cycles of galvanostatic charge−discharge cycling. However, excess Sn in SnSb phase (as in SnSb-75-25-CF) helps in improving the specific capacity compared to that of SnSb-50-50-CF. The specific capacity for SnSb-75-25-CF is 600 mAh g^{-1} after 50 cycles and 552 mAh g^{-1} after 100 cycles. The capacity fading of SnSb-75-25-CF (cf. Figure 6c) is slightly higher (~14.8% at the 50th cycle with respect to the second discharge capacity

DOI: 10.1021/acsomega.7b01479
ACS Omega 2017, 2, 9250−9260

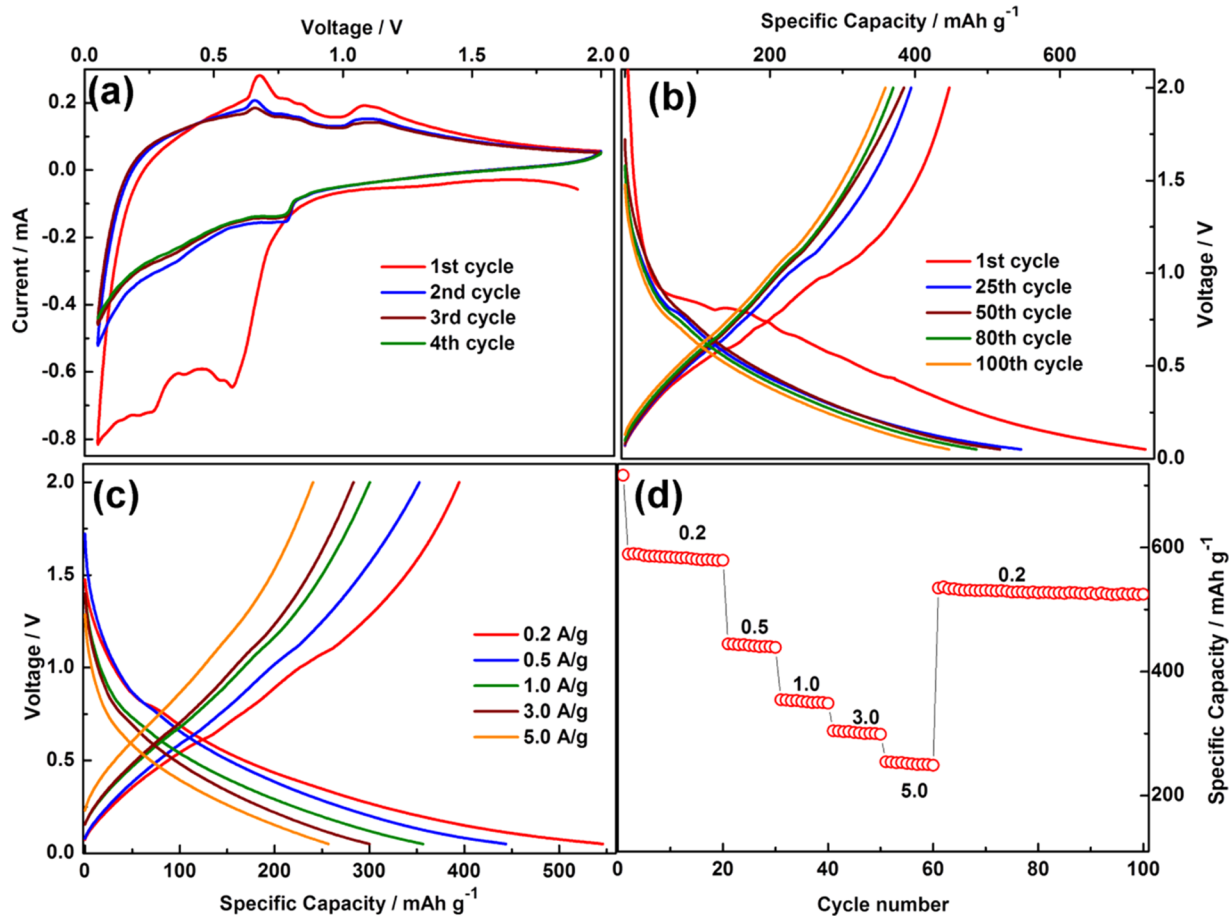

Figure 5. (a) Cyclic voltammogram (at a scan rate = 0.1 mV s^{-1}) (b) galvanostatic charge−discharge voltage profiles for different cycle numbers (current rate density = 0.2 A g^{-1}) and the second cycle at different current rate densities: 0.2−5.0 A g^{-1}, (c) capacity versus cycle number plot of and (d) rate capability of SnSb-50-50-CF versus Li^+|Li.

and 7.3% between 50 and 100 cycles) compared to that of SnSb-50-50-CF (∼13.8% at 50th cycle compared to second discharge capacity and ∼4.4% in between 50 and 100 cycles). Figure 7 represents the electrochemical performance of SnSb series of compound as a function of the percentage of Sn presence in the compounds. It is found that after 100 cycles, SnSb-75-25-CF delivers the highest capacity. The superior performance of SnSb-75-25-CF over that of SnSb-50-50-CF can be explained by comparing the anodic current regime of cyclic voltammogram (Figure 7b). Because the failure mechanism of SnSb is associated with the loss of Sn and corresponding formation of Sb from Li_3Sb, a careful analysis of the voltage range (1.0−1.2 V) becomes necessary. In SnSb-50-50-CF, as a consequence of incomplete formation of SnSb at approximately 1.08 V due to less availability of Sn, a prominent peak of Li_3Sb-to-Sb conversion appears approximately at 1.14 V. Unlike SnSb-50-50-CF, the peak of Li_3Sb-to-Sb formation at 1.14 V is absent in SnSb-75-25-CF. This suggests that there is no excess Li_3Sb phase and there is complete formation of SnSb phase. The presence of extra Sn in close proximity of SnSb particles replenishes the loss of Sn while charging to form SnSb. In the case of SnSb-25-75-CF, two peaks can be observed within 1.0−1.2 V range, with slight changes in the potential and are mainly dominated by the Li_3Sb-to-Sb formation peak, as the amount of Sb present in the compound is higher compared to that of SnSb particles.

In addition to the evidence provided by the cyclic voltammograms, the complete reformation of SnSb in presence of excess Sn (as in SnSb-75-25-CF) is also supported by the dQ/dV versus voltage (V) plots obtained from the galvanostatic voltage profile of the first charge (Figure S7). The peaks observed at 0.98 and 1.04 V in the dQ/dV versus voltage (V) plot are similarly observed in the cyclic voltammogram of SnSb-50-50-CF compound, where no excess Sn is present. Similar observations have also been reported in the literature. However, in the presence of excess Sn, as in SnSb-75-25-CF, the dQ/dV versus voltage (V) plot gives rise to only one peak, indicating complete reformation of SnSb. This is also in accordance with the cyclic voltammogram of SnSb-75-25-CF. To identify Sb as the final product of delithiation from excess Li_3Sb, ex situ powder XRD was carried out (Figure S8). However, no signatures of Sb in the ex situ powder XRD pattern for either of SnSb-50-50-CF and SnSb-75-25-CF was obtained. The absence of diffraction lines of Sb indicates that the formed Sb is amorphous in nature but electrochemically still active. This is in full accordance with published ex situ and in situ results.[31,38,44] In this context, an investigation of the morphology and microstructure of SnSb-75-25-CF following cycling is studied using SEM and TEM (Figure S9). The retention of the fibrous morphology (Figure S9a) with similar diameter of the carbon fiber composite strongly suggests that the expansion of carbon fiber is small and the particles are well dispersed inside the carbon fibers.

DOI: 10.1021/acsomega.7b01479
ACS Omega 2017, 2, 9250−9260

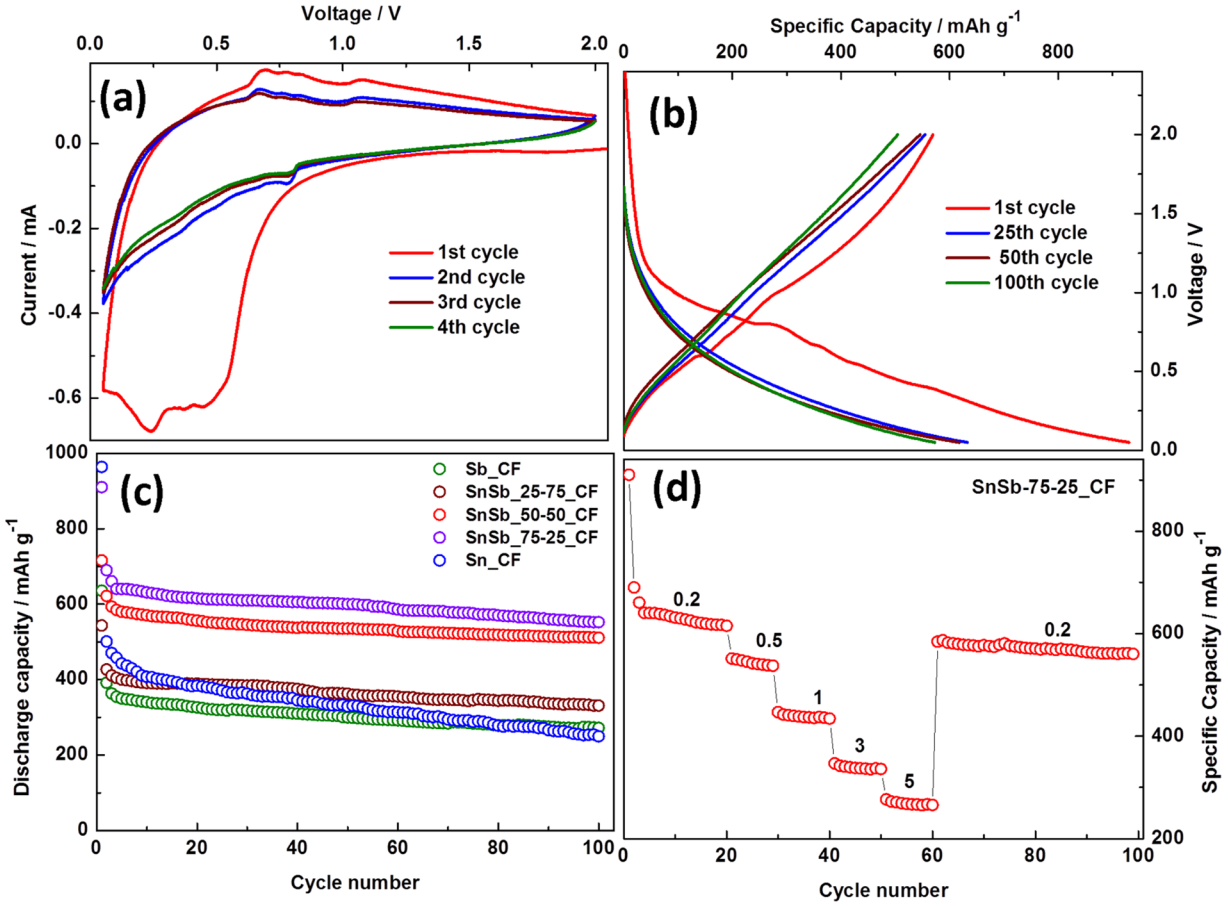

Figure 6. (a) Cyclic voltammogram (at 0.1 mV s^{-1}) and (b) galvanostatic charge−discharge voltage profiles for different cycle numbers of SnSb-75-25-CF versus $Li^+|Li$ (at 0.2 A g^{-1}). (c) Capacity versus cycle number plot of all compositions (at 0.2 A g^{-1}) and (d) rate capability of SnSb-75-25-CF versus $Li^+|Li$ (current rate densities: 0.2−5 A g^{-1}).

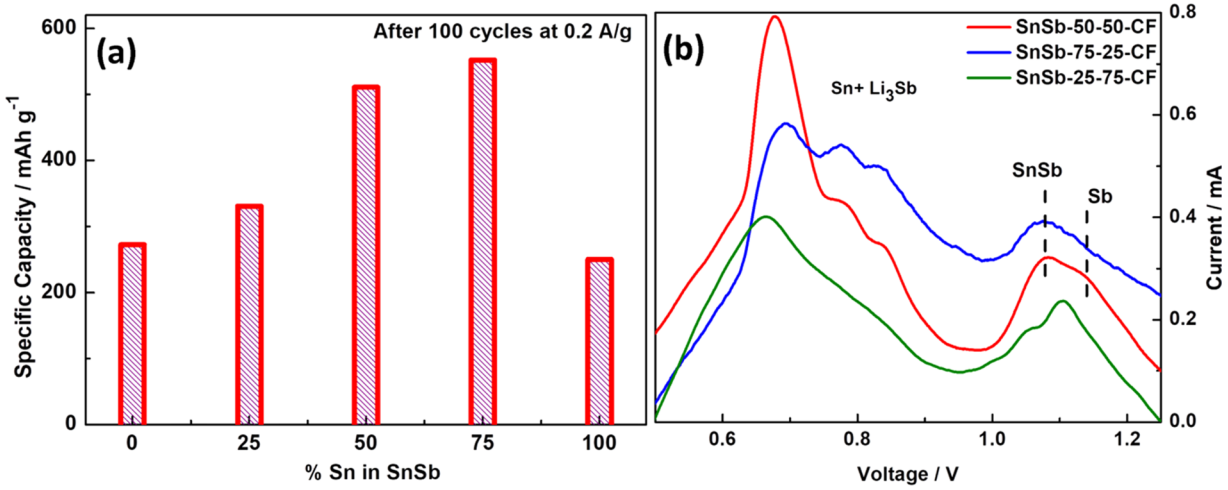

Figure 7. (a) Bar diagram of specific capacity versus the percentage of Sn present in SnSb series of compounds. Percentages of Sn present are 0, 25, 50, 75, and 100% in Sb-CF, SnSb-25-75-CF, SnSb-50-50-CF, SnSb-75-25-CF, and Sn-CF, respectively. (b) Comparison of anodic current regime of cyclic voltammogram of SnSb-50-50-CF, SnSb-75-25-CF, and SnSb-25-75-CF.

This is evident from the postcycling bright field TEM image of SnSb-75-25-CF (Figure S9b). Moreover, the particle size remains similar inside the fiber host, which suggests that the agglomeration of Sn or SnSb particles is minimal. The agglomeration of Sn or SnSb particles is restricted due to encapsulation of the particles inside the carbon fiber. Additionally, encapsulation of particles inside the porous CF (average pore size distribution of 2−5 nm and the pore volume is 0.065 cm^3 g^{-1})[26] is highly beneficial as it fully controls the volume expansion of the particles during continuous battery cycling. Thus, no special binders, such as such as poly(acrylic acid) or carboxy methyl cellulose, are employed here in the work. Poly(vinylidene fluoride) (PVDF), a commonly used

DOI: 10.1021/acsomega.7b01479
ACS Omega 2017, 2, 9250−9260

binder, is used and is sufficient for holding the carbon fiber composite to the copper current collector.

CONCLUSIONS

In conclusion, various molar ratios of Sn to Sb in SnSb particles encapsulated within an electrospun carbon fiber matrix have been investigated as prospective anode material for lithium-ion battery. The percentage of Sn present in the sample is crucial for the redox activity and eventually for the battery performance. Equal molar fractions of Sn and Sb result in irreversible loss of Sn during lithiation, resulting in incomplete reformation of SnSb particles during the charging (delithiation) process. The presence of extra Sn in close proximity with SnSb particles is necessary for the reformation of SnSb completely during changing. Fulfilling this extra requirement of Sn, SnSb-75-25-CF exhibits the best battery performance compared with SnSb-50-50-CF, which contains only pure SnSb phase. It is envisaged that the study presented here will aid in the improvement of performance of other reported intermetallic/alloy of group IV elements, where detailed concentration-dependent studies have not been performed. The alloying form of storage is equally important for electrochemical storage chemistries beyond lithium, and this study will definitely aid in screening chemical compositions, leading to stable cyclability over a wide range of currents. The findings here are also expected to be of relevance to battery material databases where compound properties are estimated from various theoretical models.[45]

EXPERIMENTAL SECTION: MATERIALS AND METHODS

Synthesis of Materials. The SnSb−carbon fiber composites are synthesized using the electrospinning technique using the optimized parameters and sintering method described in our previous work, ref 26. First, 0.4 g of polyacrylonitrile (PAN; MW = 150 000, Aldrich) is dissolved in 4 mL of dimethylformamide (DMF, Spectrochem Pvt. Ltd.) by stirring the solution for 8 h at 70 °C. Separately, another solution is prepared by dissolving various amounts of $SnCl_2$ and $SbCl_3$ in 4 mL of DMF by stirring for 2 h. The two solutions are mixed together and stirred for 8 h to obtain the precursor solution for electrospinning. The solution is loaded in a 5 mL syringe, and the needle of the syringe is connected to the high-voltage power supply of the electrospinning setup (Physics Equipments Co., Chennai, India). The flow rate of the solution is maintained at 0.5 mL h^{-1}, and the voltage difference between the tip of the needle and the aluminum sheet-covered metallic drum collector is kept at 18 kV. The distance between the needle and collector is kept at 15 cm. A Taylor cone is formed at the tip of the needle due to the electrostatic attraction between the oppositely charged needle and drum collector, followed by the polymer jet formation that gets dried in air and collected on the rotating drum (~2000 rpm). This results in a formation of a white polymer mat composed of PAN and the metal chlorides. The mat is removed from the aluminum sheet and stabilized at 280 °C in air (oxygen) for 3 h at a heating rate of 5 °C min^{-1}. The resultant brownish composite is again heat-treated at 700 °C for 3 h at the same heating rate in a reducing atmosphere maintained by flowing Ar/H_2 (95:5, v/v) to obtain nanoparticles-embedded graphitic carbon fibers. The molar ratio of $SnCl_2$ and $SbCl_3$ is taken as 0:100, 25:75, 50:50, 75:25, and 100:0 and the final compound correspondingly termed as Sb-CF, SnSb-25-75-CF, SnSb-50-50-CF, SnSb-75-25-CF, and Sn-CF, respectively.

Instrumentation and Methods. The powder X-ray diffraction patterns of the as-synthesized samples are recorded using a Philips X'pert diffractometer (nickel filter fitted) using Cu Kα radiation, (λ = 1.5418 Å, voltage = 40 kV; current = 30 mA) in the 2θ range of 20−80°. A Mettler Toledo thermogravimetric system is used to perform thermogravimetric analysis (TGA) from room temperature (30 °C) to 700 °C, with a heating rate of 5 °C min^{-1} under oxygen atmosphere. A Perkin Elmer Fourier transform infrared spectrometer with Spectrum 2000 software is used to record Fourier transform infrared spectra (FTIR) at a spectral resolution of 4 cm^{-1}. A LabRam HR system with a 532 nm diode pump solid-state laser has been used to collect the Raman spectra of the as-synthesized samples. Scanning electron microscopy (SEM) has been performed on a FEI FEG 250 ESEM machine. Transmission electron microscopy (TEM) and high resolution transmission electron microscopy (HRTEM) are recorded on JEOL 2100F (equipped with field emission gun). Cyclic voltammetry of the samples is carried using CH-Instruments (CH608C) in the voltage range of 0.05−2.0 V at a scan rate of 0.1 mV s^{-1}. Arbin Corp. (model BT 2000) is used for galvanostatic charge/discharge cycling at different current densities ranging from 0.2 to 5 A g^{-1} in the voltage range of 0.05−2.0 V (versus Li^+/Li).

Electrochemical Cell Assembly. The electrochemical properties of the electrode materials in the Li-battery configuration are extensively studied using Swagelok cells with 1 M $LiPF_6$ in a 1:1 volume ratio of ethylene carbonate and dimethyl carbonate as electrolyte, lithium foil (Aldrich, thickness = 0.75 mm) as a counter and reference electrodes, and absorptive glass mat as the separator. A slurry is first prepared with the electroactive material and poly(vinylidene fluoride) (PVDF, Kynarflex) in the weight ratio of 90:10 in cyclopentanone. No additional carbon is used as the electroactive material itself contains graphitic carbon fibers that serve the role of electrical conduits. The slurry is cast on a battery-grade high-purity clean copper foil and dried overnight at atmospheric temperature. All cell assemblies are done inside a glovebox (MBraun) under argon atmosphere (H_2O < 0.5 ppm, O_2 < 0.5 ppm).

ASSOCIATED CONTENT

Supporting Information

The Supporting Information is available free of charge on the ACS Publications website at DOI: 10.1021/acsomega.7b01479.

Figures S1−S9 of Raman spectra, SEM, and TEM images; cyclic voltammogram and galvanostatic charge−discharge cycling of Sb-CF, SnSb-25-75-CF, and Sn-CF against $Li^+|Li$; dQ/dV versus V plot; ex situ powder XRD pattern; and after-cycling SEM and TEM data (PDF)

AUTHOR INFORMATION

Corresponding Authors

*E-mail: gururow@iisc.ac.in (T.N.G.R.).
*E-mail: aninda_jb@iisc.ac.in (A.J.B.).

ORCID

Tayur N. Guru Row: 0000-0001-7830-9532
Aninda J. Bhattacharyya: 0000-0002-0736-0004

DOI: 10.1021/acsomega.7b01479
ACS Omega 2017, 2, 9250−9260

Funding

A.J.B. acknowledges the support of DST-SERI (DST/TM/SERI/FR/100(G) Date: 28/05/2015), Government of India, AISRF and STC-ISRO-IISc (STC/P-391, Dt. 28.3.17) and AISRF (DST/INT/AUS/P-71/2016; Dt. 6.6.16) for financial support.

Notes

The authors declare no competing financial interest.

■ ACKNOWLEDGMENTS

Authors acknowledge Solid State and Structural Chemistry Unit, Indian Institute of Science, Bangalore and Centre for Excellence in Nano Science and Engineering (CENSE), Indian Institute of Science, Bangalore for all infrastructural support. S.D. acknowledges the University Grants Commission (UGC) for providing Senior Research Fellowship.

■ REFERENCES

(1) Armaroli, N.; Balzani, V. Towards an electricity-powered world. *Energy Environ. Sci.* **2011**, *4*, 3193−3222.
(2) Goodenough, J. B.; Park, K.-S. The Li-Ion Rechargeable Battery: A Perspective. *J. Am. Chem. Soc.* **2013**, *135*, 1167−1176.
(3) Ellis, B. L.; Lee, K. T.; Nazar, L. F. Positive Electrode Materials for Li-Ion and Li-Batteries. *Chem. Mater.* **2010**, *22*, 691−714.
(4) Rezvani, S. J.; Ciambezi, M.; Gunnella, R.; Minicucci, M.; Muñoz, M. A.; Nobili, F.; Pasqualini, M.; Passerini, S.; Schreiner, C.; Trapananti, A.; Witkowska, A.; Cicco, A. D. Local Structure and Stability of SEI in Graphite and ZFO Electrodes Probed by As K-Edge Absorption Spectroscopy. *J. Phys. Chem. C* **2016**, *120*, 4287−4295.
(5) Liu, Q.; Du, C.; Shen, B.; Zuo, P.; Cheng, X.; Ma, Y.; Yin, G.; Gao, Y. Understanding undesirable anode lithium plating issues in lithium-ion batteries. *RSC Adv.* **2016**, *6*, 88683−88700.
(6) Nitta, N.; Wu, F.; Lee, J. T.; Yushin, G. Li-Ion battery materials: present and Future. *Mater. Today* **2015**, *18*, 252−264.
(7) Nitta, N.; Yushin, G. High-Capacity Anode Materials for Lithium-Ion Batteries: Choice of Elements and Structures for Active Particles. *Part. Part. Syst. Charact.* **2014**, *31*, 317−336.
(8) Praneetha, S.; Murugan, A. V. Development of Sustainable Rapid Microwave Assisted Process for Extracting Nanoporous Si from Earth Abundant Agricultural Residues and Their Carbon-based Nano-hybrids for Lithium Energy Storage. *ACS Sustainable Chem. Eng.* **2015**, *3*, 224−236.
(9) Tian, H.; Xin, F.; Wang, X.; He, W.; Han, W. High capacity group-IV elements (Si, Ge, Sn) based anodes for lithium-ion batteries. *J. Materiomics* **2015**, *1*, 153−169.
(10) Yoon, T.; Nguyen, C. C.; Seo, D. M.; Lucht, B. L. Capacity Fading Mechanisms of Silicon Nanoparticle Negative Electrodes for Lithium Ion Batteries. *J. Electrochem. Soc.* **2015**, *162*, A2325−A2330.
(11) Beaulieu, L. Y.; Eberman, K. W.; Turner, R. L.; Krause, L. J.; Dahn, J. R. Colossal Reversible Volume Changes in Lithium Alloys. *Electrochem. Solid-State Lett.* **2001**, *4*, A137−A140.
(12) Lee, K. T.; Jung, Y. S.; Oh, S. M. Synthesis of Tin-Encapsulated Spherical Hollow Carbon for Anode Material in Lithium Secondary Batteries. *J. Am. Chem. Soc.* **2003**, *125*, 5652−5653.
(13) Shiva, K.; Kiran, M. S. R. N.; Ramamurty, U.; Asokan, S.; Bhattacharyya, A. J. A broad pore size distribution mesoporous SnO_2 as anode for lithium-ion batteries. *J. Solid State Electrochem.* **2012**, *16*, 3643−3649.
(14) Shiva, K.; Jayaramulu, K.; Rajendra, H. B.; Maji, T. K.; Bhattacharyya, A. J. In-situ Stabilization of Tin Nanoparticles in Porous Carbon Matrix derived from Metal Organic Framework: High Capacity and High Rate Capability Anodes for Lithium-ion Batteries. *Z. Anorg. Allg. Chem.* **2014**, *640*, 1115−1118.
(15) Liu, L.; Xie, F.; Lyu, J.; Zhao, T.; Li, T.; Choi, B. G. Tin-based anode materials with well-designed architectures for next generation lithium-ion batteries. *J. Power Sources* **2016**, *321*, 11−35.
(16) Deng, Y.; Fang, C.; Chen, G. The developments of SnO2/graphene nanocomposites as anode materials for high performance lithium ion batteries: A review. *J. Power Sources* **2016**, *304*, 81−101.
(17) Zhao, Y.; Li, X.; Yan, B.; Li, D.; Lawes, S.; Sun, X. Significant impact of 2D graphene nano sheets on large volume change tin-based anodes in lithium-ion batteries: A review. *J. Power Sources* **2015**, *274*, 869−884.
(18) Wang, X.-L.; Han, W.-Q.; Chen, J.; Graetz, J. Single-Crystal Intermetallic M−Sn (M = Fe, Cu, Co, Ni) Nanospheres as Negative Electrodes for Lithium-Ion Batteries. *ACS Appl. Mater. Interfaces* **2010**, *2*, 1548−1551.
(19) Eftekhari, A. Lithium-Ion Batteries with High Rate Capabilities. *ACS Sustainable Chem. Eng.* **2017**, *5*, 2799−2816.
(20) Alcántara, R.; Nwokeke, U.; Rodríguez, I.; Tirado, J. L. Electrochemical Reaction of Lithium with Nanocrystalline $CoSn_3$. *Electrochem. Solid-State Lett.* **2008**, *11*, A209−A213.
(21) Hassoun, J.; Panero, S.; Simon, P.; Taberna, P. L.; Scrosati, B. High-Rate, Long-Life Ni−Sn Nanostructured Electrodes for Lithium-Ion Batteries. *Adv. Mater.* **2007**, *19*, 1632−1635.
(22) Shin, H.-C.; Liu, M. Three-Dimensional Porous Copper-Tin Alloy Electrodes for Rechargeable Lithium Batteries. *Adv. Funct. Mater.* **2005**, *15*, 582−586.
(23) Sengupta, S.; Patra, A.; Akhtar, M.; Das, K.; Majumder, S. B.; Das, S. 3D microporous Sn-Sb-Ni alloy impregnated Ni foam as high-performance negative electrode for lithium-ion batteries. *J. Alloys Compd.* **2017**, *705*, 290−300.
(24) Guo, H.; Zhao, H.; Yin, C.; Qiu, W. Si/SnSb alloy composite as high capacity anode materials for Li-ion batteries. *J. Alloys Compd.* **2006**, *426*, 277−280.
(25) Needham, S. A.; Wang, G. X.; Liu, H. K. Electrochemical performance of SnSb and Sn/SnSb nanosize powders as anode materials in Li-ion cells. *J. Alloys Compd.* **2005**, *400*, 234−238.
(26) Shiva, K.; Rajendra, H. B.; Bhattacharyya, A. J. Electrospun SnSb Crystalline Nanoparticles inside Porous Carbon Fibers as a High Stability and Rate Capability Anode for Rechargeable Batteries. *ChemPlusChem* **2015**, *80*, 516−521.
(27) Walter, M.; Doswald, S.; Kovalenko, M. V. Inexpensive colloidal SnSb nanoalloys as efficient anode materials for lithium- and sodium-ion batteries. *J. Mater. Chem. A* **2016**, *4*, 7053−7059.
(28) Tang, X.; Yan, F.; Wei, Y.; Zhang, M.; Wang, T.; Zhang, T. Encapsulating Sn_xSb Nanoparticles in Multichannel Graphene-Carbon Fibers As Flexible Anodes to Store Lithium Ions with High Capacities. *ACS Appl. Mater. Interfaces* **2015**, *7*, 21890−21897.
(29) Park, C. M.; Jeon, K.-J. Porous structured SnSb/C nanocomposites for Li-ion battery anodes. *Chem. Commun.* **2011**, *47*, 2122−2124.
(30) He, M.; Walter, M.; Kravchyk, K. V.; Erni, R.; Widmer, R.; Kovalenko, M. V. Monodisperse SnSb nanocrystals for Li-ion and Na-ion battery anodes: synergy and dissonance between Sn and Sb. *Nanoscale* **2015**, *7*, 455−459.
(31) Park, C. M.; Sohn, H.-J. A mechano- and electrochemically controlled SnSb/C nanocomposite for rechargeable Li-ion batteries. *Electrochim. Acta* **2009**, *54*, 6367−6373.
(32) Zhao, H.; Yin, C.; Guo, H.; Qiu, W. Microcrystalline SnSb Alloy Powder as Lithium Storage Material for Rechargeable Lithium-Ion Batteries. *Electrochem. Solid-State Lett.* **2006**, *9*, A281−A284.
(33) Seo, J.-U.; Park, C. M. Nanostructured SnSb/MOx (M 1/4 Al or Mg)/C composites: hybrid mechanochemical synthesis and excellent Li storage performances. *J. Mater. Chem. A* **2013**, *1*, 15316−15322.
(34) Nithyadharseni, P.; Reddy, M. V.; Nalini, B.; Chowdari, B. V. R. Electrochemical investigation of SnSb nano particles for lithium-ion batteries. *Mater. Lett.* **2015**, *150*, 24−27.
(35) Darwiche, A.; Sougrati, M. T.; Fraisse, B.; Stievano, L.; Monconduit, L. Facile synthesis and long cycle life of SnSb as negative electrode material for Na-ion batteries. *Electrochem. Commun.* **2013**, *32*, 18−21.
(36) Xiao, L.; Cao, Y.; Xiao, J.; Wang, W.; Kovarik, L.; Niea, Z.; Liu, J. High capacity, reversible alloying reactions in SnSb/C nano-

DOI: 10.1021/acsomega.7b01479
ACS Omega 2017, 2, 9250−9260

composites for Na-ion battery applications. *Chem. Commun.* **2012**, *48*, 3321−3323.
(37) Chen, C.; Fu, K.; Lu, Y.; Zhu, J.; Xue, L.; Hua, Y.; Zhang, X. Use of a tin antimony alloy-filled porous carbon nanofiber composite as an anode in sodium-ion batteries. *RSC Adv.* **2015**, *5*, 30793−30800.
(38) Antitomaso, P.; Fraisse, B.; Stievano, L.; Biscaglia, S.; Perrot, D. A.; Girard, P.; Sougratiab, M. T.; Monconduit, L. SnSb electrodes for Li-ion batteries: the electrochemical mechanism and capacity fading origins elucidated by using operando techniques. *J. Mater. Chem. A* **2017**, *5*, 6546−6555.
(39) Sun, W.; Lu, X.; Tong, Y.; Lei, J.; Nie, G.; Wang, C. A one-pot synthesis of a highly dispersed palladium/polypyrrole/polyacrylonitrile nanofiber membrane and its recyclable catalysis in hydrogen generation from ammonia borane. *J. Mater. Chem. A* **2014**, *2*, 6740−6746.
(40) Dalton, S.; Heatley, F.; Budd, P. M. Thermal stabilization of polyacrylonitrile fibres. *Polymer* **1999**, *40*, 5531−5543.
(41) Li, J.; Su, S.; Zhou, L.; Abbot, A. M.; Ye, H. Dielectric transition of polyacrylonitrile derived carbon nanofibers. *Mater. Res. Express* **2014**, *1*, No. 035604.
(42) Gnanaraj, J. S.; Levi, M. D.; Levi, E.; Salitra, G.; Aurbach, D.; Fischer, J. E.; Claye, A. Comparison Between the Electrochemical Behavior of Disordered Carbons and Graphite Electrodes in Connection with Their Structure. *J. Electrochem. Soc.* **2001**, *148*, A525−A536.
(43) Ramireddy, T.; Rahman, M. M.; Xing, T.; Chen, Y.; Glushenkov, A. M. Stable anode performance of an Sb−carbon nanocomposite in lithium-ion batteries and the effect of ball milling mode in the course of its preparation. *J. Mater. Chem. A* **2014**, *2*, 4282−4291.
(44) Fernández-Madrigal, F. J.; Lavela, P.; Vicente, C. P.; Tirado, J. L.; et al. X-ray Diffraction, 7Li MAS NMR Spectroscopy, and ^{119}Sn Mössbauer Spectroscopy Study of SnSb-Based Electrode Materials. *Chem. Mater.* **2002**, *14*, 2962−2968.
(45) Material Genome Initiative. https://www.mgi.gov/.

DOI: 10.1021/acsomega.7b01479
ACS Omega 2017, 2, 9250−9260